Electronic Supplementary Material (ESI) for Physical Chemistry Chemical Physics.

Electronic supporting information (ESI):

Enhanced electrochemical hydrogen oxidation reaction and suppressed hydrogen peroxide generation properties of Pt/Ir(111) bimetallic surfaces

Kenta Hayashi,* Takeru Tomimori, Riku Sato, Naoto Todoroki, and Toshimasa Wadayama

AUTHOR ADDRESS: Graduate School of Environmental Studies, Tohoku University, Sendai 980-8579, JAPAN

*Corresponding author, E-mail: kenta.hayashi.r8@dc.tohoku.ac.jp

A. Explanation for estimation of Pt coverage from X-ray photoelectron spectroscopy (XPS)

The amount of Pt deposited on the Ir(111) substrate (MaTeck, 99.999%, miscut angle < 0.1°) surface can be quantified based on pre-experiment using XPS.[1] The same methodology was utilized by Yang et al., who quantified the amount of the Pt deposited on the Ir polycrystalline substrate.[2] Layer-by-layer growth of Pt, constant Pt deposition rate, and fixed emission angle are assumed in the following discussion.

Hereafter, the photoelectron intensity from *n* monolayer (ML) Pt (*n* = 1, 2, 3,…) is written as $I_{Pt}(d_{nML})$, and can be considered as a function of the thickness of *n* ML Pt, d_{nML}. For the growth of the first Pt layer on the Ir(111) surface, the photoelectron intensity from Pt, $I_{Pt,\alpha_{1st}}$, can be written as:

$$I_{Pt,\alpha_{1st}} = \alpha_{1st} I_{Pt}(d_{1ML}) \#(1)$$

Where α_{1st} ($0 < \alpha_{1st} < 1$) is the coverage of the first Pt layer. As shown in eq.(1), $I_{Pt,\alpha_{1st}}$ increases linearly with α_{1st}, and the slope ($\Delta I_{Pt,\alpha_{1st}}/\Delta\alpha_{1st}$) is $I_{Pt}(d_{1ML})$. For the growth of the second Pt layer with coverage of α_{2nd} ($0 < \alpha_{2nd} < 1$), the photoelectron intensity from Pt, $I_{Pt,\alpha_{2nd}}$, can be written as:

$$I_{Pt,\alpha_{2nd}} = \alpha_{2nd} I_{Pt}(d_{2ML}) + (1 - \alpha_{2nd}) I_{Pt}(d_{1ML})$$
$$= \alpha_{2nd}\{I_{Pt}(d_{2ML}) - I_{Pt}(d_{1ML})\} + I_{Pt}(d_{1ML}) \#(2)$$

As shown in eq.(2), $I_{Pt,\alpha_{2nd}}$ increases linearly with α_{2nd}, but the slope ($\Delta I_{Pt,\alpha_{2nd}}/\Delta\alpha_{2nd}$) is $\{I_{Pt}(d_{2ML}) - I_{Pt}(d_{1ML})\}$, which is a different value from that of the first Pt layer growth.

Therefore, a slope-break can be found by plotting the photoelectron intensity originating from Pt against deposition time (i.e., Pt coverage), corresponding to the time required to deposit just 1 ML-thick Pt. The sample preparation chamber was equipped with an XPS system (analyzer: PHOIBOS 1500, SPECS), and Mg Kα radiation was used as an X-ray source (XG-50, SPECS). The sample position was fixed throughout the experiment. During the detection of the photoelectron signal, Pt deposition was suspended by a shutter. The photoelectron intensity, peak area of $Pt4f_{7/2}$ band, was calculated by CasaXPS (Casa Software Ltd.) (Figure S.1(a)). A Shirley-type background was assumed, and the ratio of Lorentzian to Gaussian for the fitting functions was 30%. The areal intensity ratio of $Pt4f_{5/2}$ to $Pt4f_{7/2}$ was fixed to 3/4. $Pt4f_{7/2}$ peak position was found shifted to a higher binding energy side relative to clean Pt, possible due to electronic charge transfer between Pt and Ir atoms[3–5].

Additionally, Figure S.1 (b) depicts the spectra in the Ir4f region with an appropriate graph scale. Concerning the interatomic charge transfer, a positive shift of Pt 4f bands with increased Ir content for the Ir–Pt bimetallic system typically accompanies a negative shift of Ir 4f band energies,[3–5] which was, however, not observed in Figure S.1 (b). Because the photoelectron signals originating from the Ir atoms interacting with Pt atoms were overlapped by those originating from the bulk Ir substrate, one might consider that the electronic states of specific Ir surface sites would also be modified.

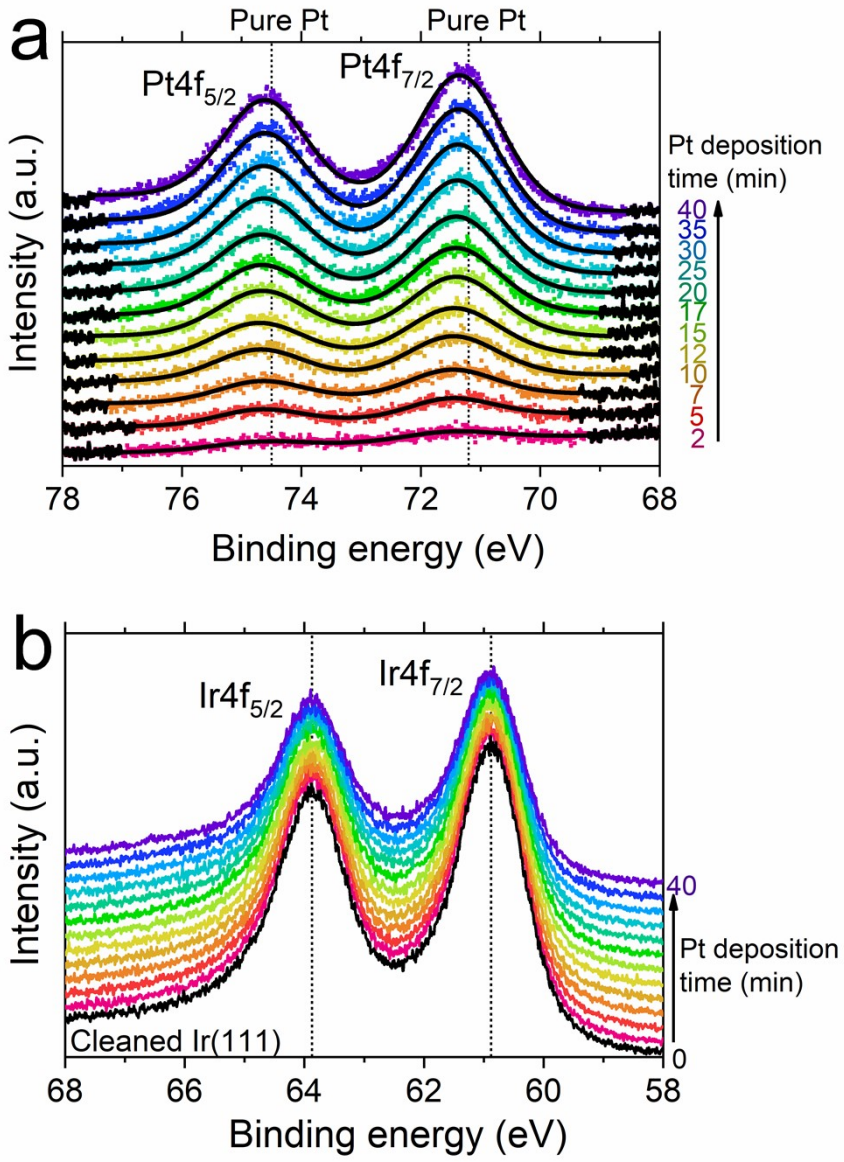

Figure S.1 Results of XPS measurements with increasing Pt deposition time on an Ir(111) substrate surface. (a) Spectra in Pt4f region with fitting results (solid lines). (b) Spectra in Ir4f region.

B. XP spectra before and after the annealing (*R.2(1)*)

The XPS measurements for UHV-fabricated $Pt_{x ML}$/Ir(111) were conducted before and after the UHV-thrmal-annealing at 673 K for 30 min. The obtained Pt4f spectra normalized by Ir4f peak intensities are shown in Figure S.2. The Pt4f intensity and the binding energy were remained unchanged by the annealing.

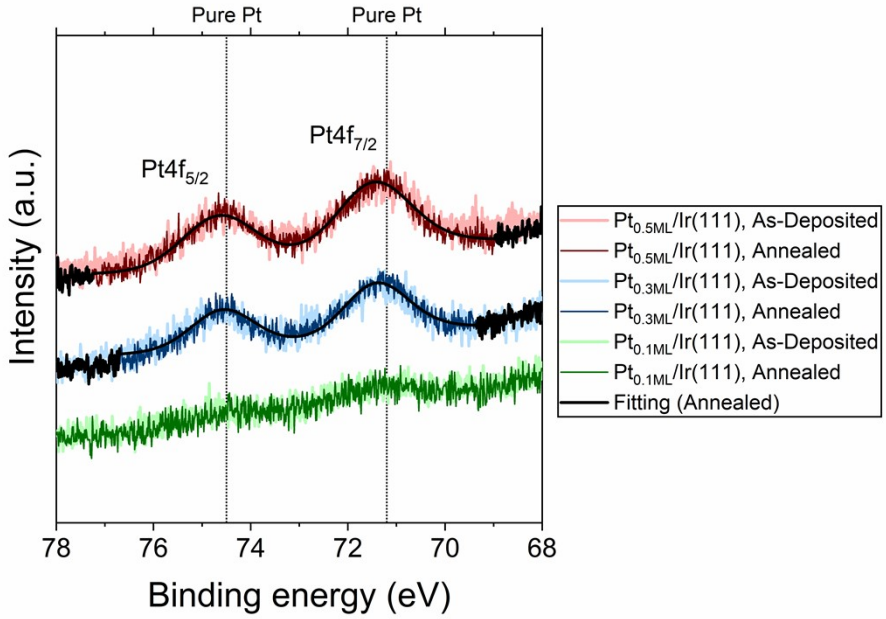

Figure S.2 XP spectra in Pt4f region abtained before (light colors) and after (dark colors) the annealing at 673 K for 30 min. Fitting results for the spectra of annealed $Pt_{0.5ML}$/Ir(111) and $Pt_{0.3ML}$/Ir(111) are displayed as black lines. Fitttings for the $Pt_{0.1ML}$/Ir(111) (for neither as-deposited nor after annealed) are not displayed due to the weak intensities and low S/N ratios.

C. Low energy electron diffraction (LEED) patterns (*R.3(1)*)

Figure S.3 shows the LEED patterns obtained for the Pt_{xML}/Ir(111) surfaces. LEED optics are installed in the same ultra-high vacuum (UHV) chamber as the sample preparations. All patterns in Figure S.3 show the diffraction spots with six-fold symmetry, though the increasing Pt deposition thickness of *x* tends to be diffuse diffraction spots.

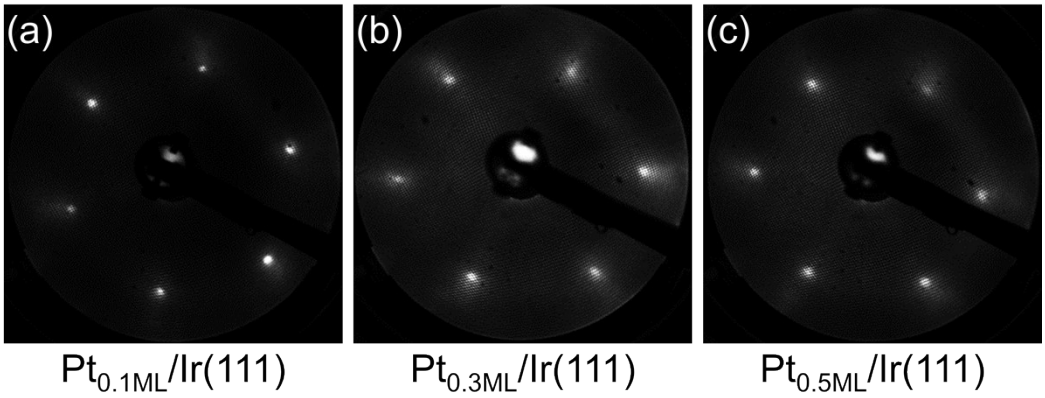

Figure S.3 LEED patterns obtained for (a) $Pt_{0.1ML}$/Ir(111), (b) $Pt_{0.3ML}$/Ir(111), and (c) $Pt_{0.5ML}$/Ir(111) surfaces. The electron energy was 100 eV, yet no effort has been made to detailed dynamical analysis of LEED spots.

D. Scanning tunneling microscopy (STM) observation

The STM system is installed in the same UHV system as the sample preparations. The STM image for $Pt_{0.3ML}$/Ir(111) collected with a typical tunneling current of 0.05 nA is shown in Figure S.4 (a). Flat terraces and island-like structures can be observed. The line profile in Figure S.4 (b) shows that the height of the island is monoatomic scale (0.2–0.3 nm), and the width is approximately 10 nm. Furthermore, many island-like structures take hexagonal shapes (Figure S.4 (a)), implying epitaxial growth of the islands on Ir(111), whose atomic arrangement has six-fold symmetry. Thus, these island-like structures should be surface Pt islands grown epitaxially. The bimetallic surface of Ir and Pt, i.e., domains of Ir and Pt co-exists, can be confirmed for $Pt_{0.3ML}$/Ir(111) from the image.

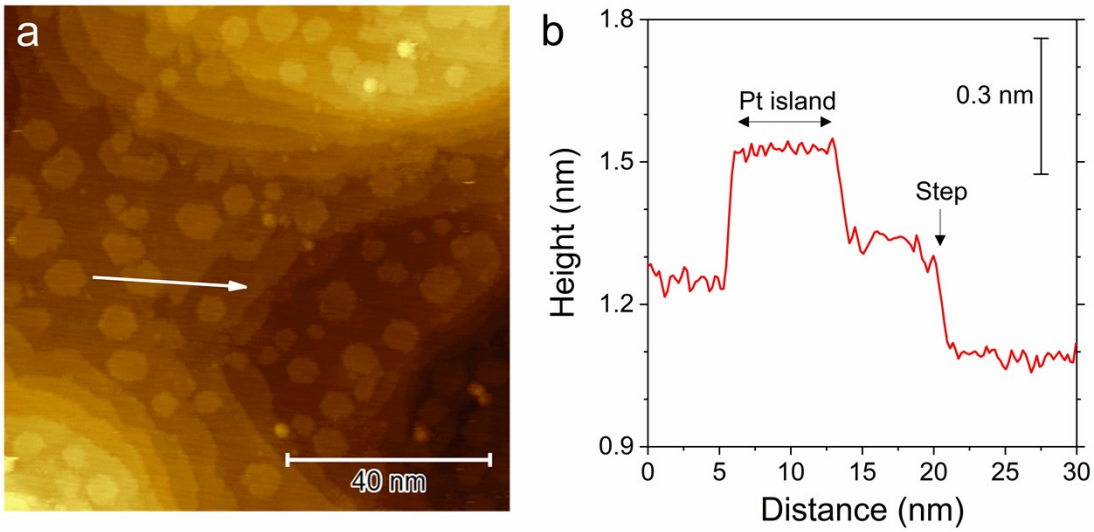

Figure S.4 (a) UHV–STM image of the $Pt_{0.3ML}$/Ir(111) surface and (b) line profile.

E. Experimental procedure for scanning electrochemical microscope (SECM) measurements and results

Experimental details were the same as those described in our previous literature.[6] The sample was first transferred from an UHV chamber to an N_2-purged glove box without air exposure.[7] The electrochemical cell was assembled in the glove box, and the sample surface was covered by N_2-purged solution. After that, the sample was transferred to the SECM system in air. For SECM measurements, an Ag/AgCl electrode (saturated KCl, Hokuto Denko) and a Pt wire (0.05-mm diameter) were used as reference electrode (RE) and countor electrode (CE), respectively. Unless otherwise stated, the estimated electrochemical potentials measured by Ag/AgCl RE (V vs. Ag/AgCl) are converted to reversible hydrogen electrode scale (V vs. RHE).[6] The geometrical surface area of the sample substrate electrodes was determined by O-ring (Kalrez, 0.062 cm^2). Solutions were prepared with lab-grade chemicals, such as $HClO_4$ (Ultrapure, Kanto Chemical) and $NaClO_4$ (Sendai Wako Pure Chemicals), and ultrapure water (18.2 MΩ cm, Mili-Q). All electrochemical measurements were conducted at room temperature (approximately 297 K).

(1) Estimation of the HOR activity

HOR activity was estimated using the tip generation/substrate collection (TG/SC) mode of the SECM in a mixed solution containing 0.01 M $HClO_4$ and 0.1 M $NaClO_4$.[8–10] A Pt ultramicroelectrode (UME) tip (diameter: ca. 25 μm, Sensolytics) was placed as close as possible to the sample substrate surface. After that, a negative going scan for the sample substrate potential (E_S) was performed at a scan rate of 5 mV/s, with the Pt UME tip potential (E_T) remaining at –0.74 V, at which the hydrogen evolution reaction (HER) proceeds, and the Pt UME tip current (i_T) was recorded. The i_T value was normalized by the limiting current for HER on the Pt UME ($i_{T\rightarrow\infty}$), which was measured by cyclic voltammetry prior to each experiment. In this TG/SC mode of the SECM, HOR rates on the sample surfaces can be fed back to the normalized Pt UME tip current ($I_T = i_T/i_{T\rightarrow\infty}$).

HOR activity was evaluated based on the standard rate constant (k^0) estimated by fitting the E_S-dependence of I_T to the theoretical equations.[11–13] Fitting parameters are k^0, apparent transfer coefficient (α_{app}), and tip-substrate distance normalized by tip radius ($L = d/a$). Figure S.5 depicts the representative experimental data (circles) and fitting results (solid lines). Measurements were conducted at three different tip positions, and the averaged values of k^0 are displayed in the main manuscript.

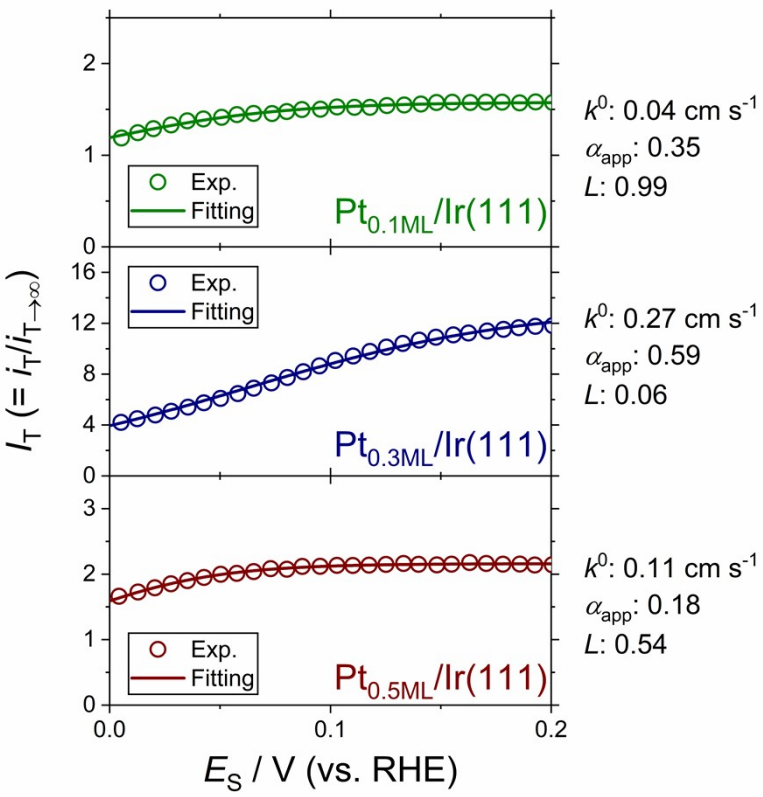

Figure S.5 Representative I_T vs. E_S curves for $Pt_{x ML}$/Ir(111). Fitting parameters are also displayed.

(2) Evaluation of H_2O_2 generation properties

H_2O_2 generation properties were evaluated by substrate generation/tip collection (SG/TC) mode of the SECM in O_2-saturated 0.1 M $HClO_4$.[14,15] After the Pt UME tip (diameter: ca. 20 μm, Hokuto Denko) was positioned to approximately 50 μm above the sample substrate surface, negative going scan for E_S was performed at 2 mV/s. During the scan, E_T was fixed to > 1.26 V to detect H_2O_2 through oxidation ($H_2O_2 \rightarrow O_2 + 2H^+ + 2e^-$). Both i_T and sample substrate current density (j_S) were recorded. Whereas j_S corresponds to the total ORR on the sample substrate surface, i_T represents the detection of H_2O_2 generated through ORR. Note that the minimum values of i_T throughout the scanned potential range are subtracted for the displayed values in Figure S.6.

The results are summarized in Figure S.6. The results for vacuum-cleaned Ir(111) (black) and Pt(111) (gray) are from our previous literature.[6] Notably, the sharp increase in $|j_S|$ (Figure S.6(b)) below 0.06 V corresponds to HER on the sample surfaces; thus, i_T (Figure S.6(a)) in such a potential range includes H_2 detection, in addition to H_2O_2 detection. Furthermore, from the viewpoint of applications in PEFC anode catalysts, suppressing H_2O_2 generation in a relatively low potential region (< 0.3 V) is of great significance. For these reasons, a potential range of 0.06 V < E_S < 0.3 V was selected to evaluate H_2O_2 generation properties in the main manuscript (Figure 3).

(***R.1(1)***) The onset potentials of ORR for $Pt_{x\mathrm{ML}}$/Ir(111) (ca. 0.85 V), around which H_2O_2 was generated, are positively shifted by ca. 0.15 V from that of the non-Pt-deposited, clean Ir(111) (ca. 0.7 V). Similar H_2O_2 generation behavior around the ORR onset potential region was reported for the electrochemically-grown Pt monolayer on Ir(111).[16] Therefore, around its ORR

onset potential region (ca. 0.85 V vs. RHE), the Pt islands present on the Ir(111) terraces seem to correlate with the H_2O_2 generation. However, from the viewpoint of applications in PEFC anode, the H_2O_2 generations in relatively high potential region of ca. 0.3 ~ 0.8 V) are less likely to induce the PEM degradation, because the PEFC anode does not experience in such potential under the normal power generation condition.

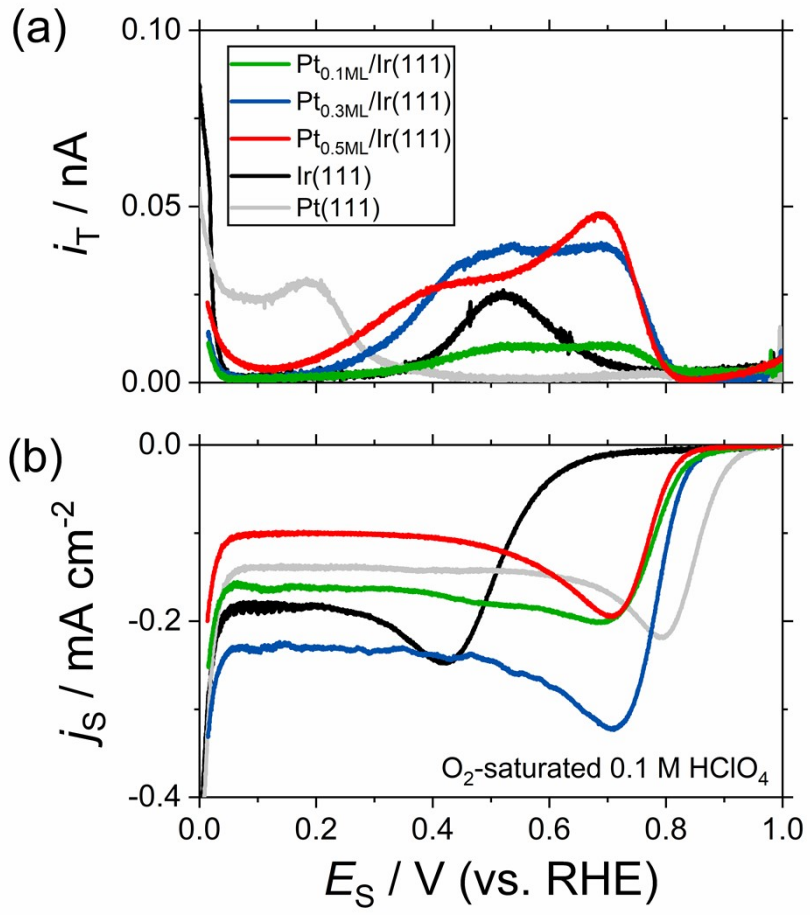

Figure S.6 E_S-dependence of (a) i_T (corresponding to H_2O_2 detection) and (b) j_S (corresponding to ORR) for $Pt_{x ML}$/Ir(111). Data for vacuum-cleaned Ir(111) (black) and Pt(111) (gray) are from our previous literature.[6]

F. Cyclic voltammograms (CVs) (*R.3(2)*)

Cyclic voltammograms (CVs) recorded in N_2-purged 0.1 M $HClO_4$ are shown in Figure S.7. CV measurements were conducted in an N_2-purged glove box after the samples were transferred from the UHV system without exposure to air.[7] A conventinal three-elctrode cell (not the cell for SECM measurements) was used. A reversible hydrogen electrode (RHE) and a Pt wire were used as the reference electrode and counter electrode, respectively. The surface area of the working electrodes was determined by an O-ring (ca. 0.09 cm^2, Kalrez, DuPont). The scan rate was 50 mV/s. The CV curves for UHV-cleaned Ir(111) and Pt(111) are also displayed in Figure S.7.

The CV shapes for $Pt_{0.1ML}$/Ir(111) and $Pt_{0.3ML}$/Ir(111) were quite similar to clean Ir(111), whereas a marked change can be observed for $Pt_{0.5ML}$/Ir(111). Particlarly, the CVs of $Pt_{0.1ML}$/Ir(111) and $Pt_{0.3ML}$/Ir(111) showed characteristic redox features around 0.95 V vs. RHE, similarly to clean Ir(111). In contrast, the redox feature cannot be observed for $Pt_{0.5ML}$/Ir(111), suggesting a half monolayer deposition of Pt on Ir(111) seriously influence surface electrochemical properties.

As for the CV features below ca. 0.4 V vs. RHE, which is known as hydrogen adsorption/desorption potential regions for Pt surfaces, the onset potential for $Pt_{0.5ML}$/Ir(111) positively shifted, compared with clean Ir(111) and Pt(111) surfaces. Even for $Pt_{0.1ML}$/Ir(111) and $Pt_{0.3ML}$/Ir(111) samples, below ca. 0.15 V vs. RHE, the current density values were higher than that of clean Ir(111). These changes in the redox features below ca. 0.4 V vs. RHE might be related to the modified hydrogen affinity of the topmost surface and, hence, the modified HOR activity. However, considering that Ir(111) adsorbs not only hydrogen but also OH-

speceis even below 0.4 V vs. RHE,[18–20] it is difficult to distinguish the electrochemical charge that stems from hydrogen adsorption from that for OH adsorption based upon the CVs features of $Pt_{x\mathrm{ML}}$/Ir(111).

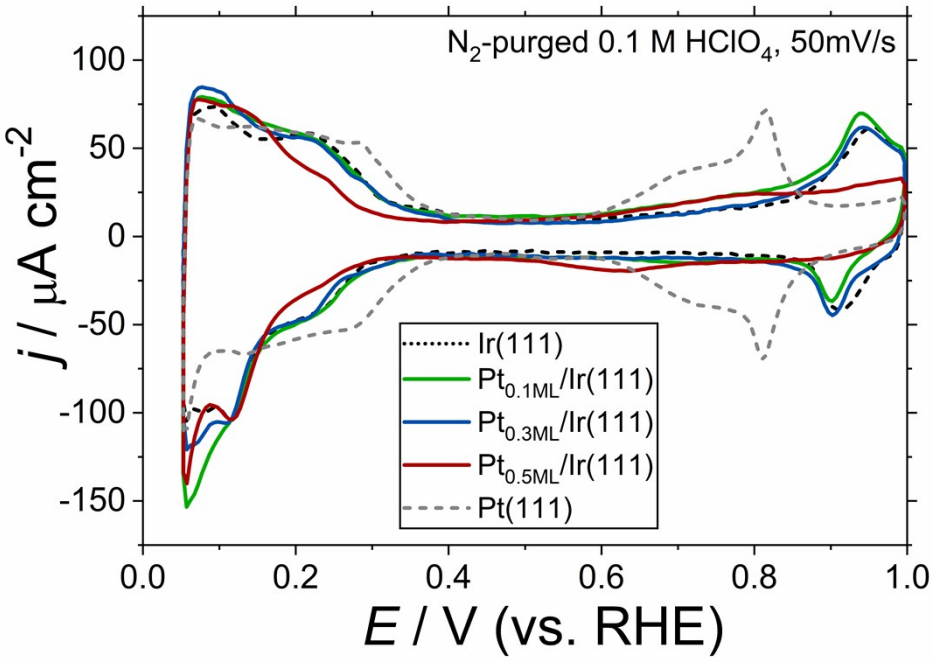

Figure S.7 CV curves recorded in N_2-purged 0.1 M $HClO_4$.

References

1 H. Siegfried, *Auger- and X-Ray Photoelectron Spectroscopy in Materials Science*, Springer, 2013.

2 X. F. Yang, W. Xu, M. Li, B. E. Koel and J. G. Chen, A new class of electrocatalysts of supporting Pt on an Engel-Brewer alloy substrate: A demonstration for oxidation of ethylene glycol, *Chem. Commun.*, 2014, **50**, 12981–12984.

3 I. Radev, G. Topalov, E. Lefterova, G. Ganske, U. Schnakenberg, G. Tsotridis and E. Slavcheva, Optimization of platinum/iridium ratio in thin sputtered films for PEMFC cathodes, *Int. J. Hydrogen Energy*, 2012, **37**, 7730–7735.

4 T. Ioroi and K. Yasuda, Platinum-Iridium Alloys as Oxygen Reduction Electrocatalysts for Polymer Electrolyte Fuel Cells, *J. Electrochem. Soc.*, 2005, **152**, A1917–A1924.

5 N. Bhuvanendran, S. Ravichandran, S. S. Jayaseelan, Q. Xu, L. Khotseng and H. Su, Improved bi-functional oxygen electrocatalytic performance of Pt–Ir alloy nanoparticles embedded on MWCNT with Pt-enriched surfaces, *Energy*, 2020, **211**, 118695.

6 K. Hayashi, T. Tomimori, Y. Chida, N. Todoroki and T. Wadayama, Hydrogen Peroxide Generation and Hydrogen Oxidation Reaction Properties of Ir(111)-, (100)-, and (110)-Low-Index Single-Crystal Surfaces, *J. Phys. Chem. C*, 2021, **125**, 21481–21487.

7 T. Wadayama, N. Todoroki, Y. Yamada, T. Sugawara, K. Miyamoto and Y. Iijama, Oxygen reduction reaction activities of Ni/Pt(111) model catalysts fabricated by molecular beam epitaxy, *Electrochem. commun.*, 2010, **12**, 1112–1115.

8 J. Zhou, Y. Zu and A. J. Bard, Scanning electrochemical microscopy - Part 39. The proton/hydrogen mediator system and its application to the study of the electrocatalysis of hydrogen oxidation, *J. Electroanal. Chem.*, 2000, **491**, 22–29.

9 C. G. Zoski, Scanning electrochemical microscopy: Investigation of hydrogen oxidation at polycrystalline noble metal electrodes, *J. Phys. Chem. B*, 2003, **107**, 6401–6405.

10 Y. C. Weng and C. T. Hsieh, Scanning electrochemical microscopy characterization of bimetallic Pt–M (M=Pd, Ru, Ir) catalysts for hydrogen oxidation, *Electrochim. Acta*, 2011, **56**, 1932–1940.

11 S. Amemiya, N. Nioradze, P. Santhosh and M. J. Deible, Generalized theory for nanoscale voltammetric measurements of heterogeneous electron-transfer kinetics at macroscopic substrates by scanning electrochemical microscopy, *Anal. Chem.*, 2011, **83**, 5928–5935.

12 C. Lefrou and R. Cornut, Analytical expressions for quantitative scanning electrochemical microscopy (SECM), *ChemPhysChem*, 2010, **11**, 547–556.

13 R. Cornut and C. Lefrou, New analytical approximation of feedback approach curves with a microdisk SECM tip and irreversible kinetic reaction at the substrate, *J. Electroanal. Chem.*, 2008, **621**, 178–184.

14 C. M. Sánchez-Sánchez and A. J. Bard, Hydrogen peroxide production in the oxygen reduction reaction at different electrocatalysts as quantified by scanning electrochemical microscopy, *Anal. Chem.*, 2009, **81**, 8094–8100.

15 A. Kishi, S. Shironita and M. Umeda, H2O2 detection analysis of oxygen reduction reaction on cathode and anode catalysts for polymer electrolyte fuel cells, *J. Power Sources*, 2012, **197**, 88–92.

16 J. Zhang, M. B. Vukmirovic, Y. Xu, M. Mavrikakis and R. R. Adzic, Controlling the catalytic activity of platinum-monolayer electrocatalysts for oxygen reduction with different substrates, *Angew. Chemie - Int. Ed.*, 2005, **44**, 2132–2135.

17 N. Todoroki, H. Watanabe, T. Kondo, S. Kaneko and T. Wadayama, Highly Enhanced Oxygen Reduction Reaction Activity and Electrochemical Stability of Pt/Ir(111) Bimetallic Surfaces, *Electrochim. Acta*, 2016, **222**, 1616–1621.

18 A. Ganassin, P. Sebast, V. Climent, W. Schuhmann, S. Aliaksandr and J. Feliu, On the pH Dependence of the Potential of Maximum Entropy of Ir (111) Electrodes, *Sci. Rep.*, 2017, **7**, 1–14.

19 K. Klyukin, A. Zagalskaya and V. Alexandrov, Ab Initio Thermodynamics of Iridium Surface Oxidation and Oxygen Evolution Reaction, *J. Phys. Chem. C*, 2018, **122**, 29350–29358.

20 M. T. M. Koper, Blank voltammetry of hexagonal surfaces of Pt-group metal electrodes: Comparison to density functional theory calculations and ultra-high vacuum experiments on water dissociation, *Electrochim. Acta*, 2011, **56**, 10645–10651.